The Relaxation Wall: Experimental Limits to Improving MPI Spatial Resolution by Increasing Nanoparticle Core size

Zhi Wei Tay[1,*], **Daniel W. Hensley**[1], **Erika C. Vreeland**[2], **Bo Zheng**[1], and **Steven M. Conolly**[1,3]

[1]Department of Bioengineering, University of California, Berkeley, USA

[2]Imagion Biosystems, Inc., Albuquerque, NM, USA

[3]Department of Electrical Engineering and Computer Sciences, University of California, Berkeley, USA

Abstract

Magnetic Particle Imaging (MPI) is a promising new tracer modality with zero attenuation in tissue, high contrast and sensitivity, and an excellent safety profile. However, the spatial resolution of MPI is currently around 1 mm in small animal scanners. Especially considering tradeoffs when scaling up MPI scanning systems to human size, this resolution needs to be improved for clinical applications such as angiography and brain perfusion. One method to improve spatial resolution is to increase the magnetic core size of the superparamagnetic nanoparticle tracers. The Langevin model of superparamagnetism predicts a cubic improvement of spatial resolution with magnetic core diameter. However, prior work has shown that the finite temporal response, or magnetic relaxation, of the tracer increases with magnetic core diameter and eventually leads to blurring in the MPI image. Here we perform the first wide ranging study of 5 core sizes between 18–32 nm with experimental quantification of the spatial resolution of each. Our results show that increasing magnetic relaxation with core size eventually opposes the expected Langevin behavior, causing spatial resolution to stop improving after 25 nm. Different MPI excitation strategies were experimentally investigated to mitigate the effect of magnetic relaxation. The results show that magnetic relaxation could not be fully mitigated for the larger core sizes and the cubic resolution improvement predicted by the Langevin was not achieved. This suggests that magnetic relaxation is a significant and unsolved barrier to achieving the high spatial resolutions predicted by the Langevin model for large core size SPIOs.

1. Introduction and Background

Magnetic Particle Imaging (MPI) is a new tracer-based molecular imaging technique that directly detects and quantifies the magnetization of superparamagnetic iron oxide (SPIO) tracers. As in other molecular imaging techniques like nuclear medicine, there is no signal from background tissue in MPI, giving MPI images high image contrast for SPIO tracers. This unique contrast mechanism, combined with the use of low-frequency magnetic fields and clinically safe magnetic tracers, enables MPI to produce clinical-grade images with zero tissue signal attenuation and high image sensitivity (Gleich et al. 2005; Patrick W Goodwill

---
*zwtay@berkeley.edu.

and Conolly 2010). As in MRI, safety in MPI is bound by magnetostimulation and specific absorption rate (SAR) safety limitations (E U Saritas et al. 2013). MPI is best compared to gold-standard tracer imaging techniques, such as nuclear medicine, but without the limitations of radiation safety or radionuclide half-life for longitudinal imaging. As such, MPI shows excellent promise for clinical applications such as angiography (Haegele et al. 2012; Salamon et al. 2016), stem cell tracking and vitality assessment (Fidler et al. 2015; Them et al. 2016; Zheng, Vazin, et al. 2015; Zheng, von See, et al. 2016), brain perfusion (Orendorff et al. 2016), lung perfusion (Zhou et al. 2016),lung ventilation (Nishimoto et al. 2015), cancer imaging (E. Yu et al. 2016), and localized hyperthermia (Murase, Aoki, et al. 2015; Hensley et al. 2016).

1.1. Working Principles of Magnetic Particle Imaging

Magnetic Particle Imaging works by exploiting the nonlinear magnetization of the superparamagnetic iron oxide (SPIO) tracers used. At any given time during a scan, strong magnetic field gradients magnetically saturate the SPIO tracers in most of the imaging field-of-view (FOV), leaving only tracers near a field-free-region (FFR) unsaturated. Only these tracers are able to respond to a superposed AC driving magnetic field, typically at 20 kHz. As a result, the detected MPI signal from an inductive pick-up coil is dominated by the tracers at the FFR, thereby localizing the signal to the FFR and forming the basis of spatial encoding in MPI. Following the x-space approach, image reconstruction can be performed by gridding the MPI signal to the instantaneous location of the FFR (Patrick W Goodwill and Conolly 2010). Because the SPIO magnetization curve is non-linear, multiple harmonics of the drive frequency are generated with the application of the drive waveform. Reconstruction can also be performed in the frequency domain by obtaining a system function and then solving the inverse problem of the spectral image data (Rahmer, Weizenecker, et al. 2009). Both methods have to discard signal at the fundamental frequency as a consequence of direct feedthrough from the excitation waveform and reconstruct from the higher harmonics. To scan the full field-of-view, strong electromagnets are used to slowly raster the FFR across the entire field-of-view. Hardware details of the MPI scanners such as the Philips-Bruker 3D Fast MPI demonstrator scanner (Rahmer, Halkola, et al. 2015) and the Berkeley x-space scanners (Patrick W Goodwill, Lu, et al. 2012; Patrick W Goodwill, Konkle, et al. 2012) have been discussed in prior work.

1.2. Spatial Resolution in Magnetic Particle Imaging

Spatial resolution in MPI is closely linked to the shape of the M-H magnetization curve of the SPIO. A steeper M-H curve results in a narrower x-space point spread function. This also implies stronger higher harmonics leading to a better modulation transfer function for frequency domain reconstruction. This results in a more well-posed inverse problem leading to better SNR and less artifacts in the reconstructed image and therefore improved effective resolution. For an ensemble of ideal superparamagnetic nanoparticles, each with magnetic moment m, the M-H curve can be described by the Langevin function as follows:

$$M(H) = Nm\, \mathscr{L}(k_{\mathrm{sat}}H) \quad (1)$$

where $\mathscr{L}(x)$ is the Langevin function which is analytically defined as $coth(x) - 1/x$. The constant k_{sat} is determined by the magnetic properties of the nanoparticle and defined as:

$$k_{sat} = \frac{\mu_0 m}{k_B T} \quad (2)$$

The steepness of the M-H curve is closely linked to m which is defined as:

$$m = \frac{M_{sat} \pi d^3}{6} \quad (3)$$

The magnetic core diameter d has a profound impact on the M-H curve and, correspondingly, spatial resolution in MPI. Previous studies on SPIO sizes from 13–19 nm have shown improved MPI resolution with increasing core size to 19 nm (Ferguson, Minard, et al. 2009; Ferguson, Khandhar, Minard, et al. 2010). Similarly, studies on the Feraspin series (size-fractionated Resovist) show improved MPI spectra with increased size-fraction (Ludwig et al. 2012).

Rahmer, Weizenecker, et al. 2009 showed that MPI spatial resolution should be inversely proportional to the cube of the magnetic core diameter using the System Matrix MPI reconstruction method. Knopp et al. 2011 also showed the width of the convolution kernel highly depends on the particle size. Precisely the same resolution limit was derived for the x-space MPI reconstruction method (Patrick W Goodwill and Conolly 2010). For x-space reconstruction, the point spread function (PSF) that defines the spatial resolution of MPI is simply the derivative of the M-H curve. One can analytically solve for the full-width-half-maximum (FWHM), which is the standard Houston resolution criterion (Houston 1927)). If the effects of magnetic relaxation are neglected, the 1D spatial resolution of MPI, for *both* System Matrix (Rahmer, Weizenecker, et al. 2009) and x-space MPI reconstruction (Patrick W Goodwill and Conolly 2010), is

$$\Delta x = \left(\frac{24 k_B T}{\mu_0 \pi M_{sat}} \right) \frac{1}{G d^3} \quad (4)$$

where G is the gradient strength in T/(μ_0m). This equation shows that MPI spatial resolution should improve *cubically* with increasing magnetic core diameter. Because resolution only scales linearly with gradient strength G, we are limited by cost, power and cooling constraints when improving MPI spatial resolution with stronger gradients (above 5 T/(μ_0m)). The gradient strength is also constrained by human safety limits, magnetostimulation and SAR limitations (E U Saritas et al. 2013). Hence, it is enormously important to investigate the limits of the resolution improvement by increasing magnetic core diameter, and this will be even more important for scaling up to a human MPI scanners.

There have been numerous works on modeling the MPI nanoparticle response (García-Palacios et al. 1998; Weizenecker et al. 2010; Weizenecker et al. 2012; Graeser et al. 2015).

Weizenecker et al. modeled the effect of anisotropy and frequency on the MPI performance for 20,25,30 nm particles. The study noted that high levels of anisotropy reduced the MPI performance to worse than the Langevin model prediction. Graeser et al. extended the Weizenecker model for 30 nm particles and showed how proper superimposition of shape semi-axis and the crystal axes during particle synthesis can give optimal MPI performance. Other research groups (L. Croft et al. 2012; L. R. Croft et al. 2016; Dieckhoff et al. 2016; Robert J Deissler et al. 2014; R J Deissler et al. 2015; Dhavalikar et al. 2016) have also modeled how MPI spatial resolution varies with NP size, and with drive field frequency and amplitude. In general, all these studies have noted that larger SPIOs have longer magnetic relaxation times. While there are a multitude of models concerning the exact physical causes of magnetic relaxation, from an imaging perspective we are most concerned about time-delays and spreading of the MPI signal that will directly impact the reconstructed image. As such, we will define magnetic relaxation using the most general definition: the non-instantaneous response of the ensemble magnetization to the applied field (L. Croft et al. 2012). The general Néel and Brownian time constants involved in magnetic relaxation can be written as follows:

$$\tau_N = N(H) \cdot \tau_0 \exp\left(\frac{KV_c}{k_B T}\right) \qquad \tau_B = B(H) \cdot \frac{3\eta V_h}{k_B T} \quad (5)$$

where $N(H)$ and $B(H)$ are functions that account for the effect of applied field, H, on the time constants.

These equations show that both relaxation mechanisms have longer time constants when the nanoparticle grows larger. When these relaxation times approach the period of the excitation waveform, a noticeable blurring effect results that reduces achievable resolution. Hence, larger NPs should improve resolution, but relaxation-induced blurring of larger NPs may obviate the improvements in spatial resolution. Here, we expand upon prior modeling work (listed above) by performing the first experimental study on the MPI imaging performance of nanoparticles across a wide range of core sizes from 18 to 32 nm. By observing these two opposing effects in practice, we determine the practical limits to improving MPI spatial resolution by increasing core size.

2. Materials and Methods

2.1. Magnetic Nanoparticles

Imagion Biosystems PrecisionMRX® superparamagnetic iron oxide nanoparticles (Imagion Biosystems, Inc. Albuquerque, NM, USA) with carboxylic acid coated outer shell and varying core diameters were used. The core is single crystalline magnetite (Fe_3O_4) for all core sizes. This is experimentally confirmed by prior work (Vreeland et al. 2015) with high resolution transmission electron microscopy (HRTEM) and X-ray diffraction. A representative data sample is found in the supplementary information of this reference. The nanoparticle shape and hence the shape anisotropy remains approximately uniform and does not change significantly with core size. This is evidenced by the TEM (JEOL 1200EX) images in Fig. 3a showing uniform spherical shape across all core sizes. The high

isoperimetric quotients tabulated in Fig. 3b show that the deviation from an ideal sphere with increasing core size is very low.

To determine the particle core size distribution, synthesized nanoparticles were analyzed using small angle X-ray scattering (SAXS) with a Rigaku SmartLab diffractometer system and SmartLab Guidance system control software. Data analysis was performed using Rigaku NANO-Solver v3.5 software that uses a spherical particle shape with a Gaussian size distribution. The spherical shape assumption was experimentally confirmed by TEM analysis (see Fig. 3b.) Statistically, SAXS is a more rigorous technique for measuring size distribution because it is possible to measure a large ensemble of particles with SAXS while TEM image analysis is practically limited to 100 – 1000 particles.

All SPIOs have same outer coating material and differ only in the magnetic core size. The core is covered by an inner monolayer of oleic acid coating and then encapsulated within a monolayer of a carboxylic acid functionalized amphiphilic polymer. The hydrodynamic diameter and zeta potential of all SPIOs was measured in deionized water pH 6.0 using a Malvern Zetasizer Nano ZS system. The zeta potentials of all SPIOs ranged between −40 and −50 mV. Hydrodynamic diameter scales with core size as described in Fig. 3a. This scaling is necessary to maintain a large enough coating buffer to prevent inter-particle aggregation.

Magnetization measurements were collected using a Quantum Design MPMS-7 SQUID magnetometer. The precise mass of iron in the sample was determined using a colorimetric assay as described previously (Vreeland et al. 2015). Magnetization curves were recorded from −4000 kA/m to +4000 kA/m at 293K. The field-dependent magnetization data was normalized to the mass of iron in the sample to determine the saturation magnetization (σ_{sat}). The measured saturation magnetization is $M_{sat} = 0.551 \, T/\mu_0$ which is ~ 92% of the bulk magnetite value of $0.6 \, T/\mu_0$ (Cullity et al. 2011). A representative M vs. H magnetization plot (25.0 nm particles) is also plotted in Fig. 3b. The exact synthesis and more characterization of the nanoparticles can be found in detail in the main article and supplementary information of (Vreeland et al. 2015). The MPI performance of the SPIOs was also measured using a magnetic particle spectrometer/relaxometer described in (Tay, Patrick Goodwill, et al. 2016) as well as the x-space MPI scanner described in (L. R. Croft et al. 2016). Unless otherwise stated, all experimental measurements employed 25 μL SPIOs at 5 mg Fe/mL.

2.2. Magnetic Particle Relaxometer Experiments

The SPIOs of different core sizes were first tested on our arbitrary waveform relaxometer (AWR) which is described in detail in our prior work (Tay, P W Goodwill, et al. 2015; Tay, Patrick Goodwill, et al. 2016). The AWR includes a non-resonant transmit coil design to enable frequency agility as well as arbitrary excitation waveforms. This tabletop system does not have gradient fields for signal localization; instead, a sinusoidal excitation and linear bias field are superimposed to test the aggregate response of a sample in the applied magnetic field space. This system can reconstruct a 1D point-spread function (PSF) characteristic of the entire sample supplied to the device. To interrogate the entire Langevin M-H curve and even up to the saturation regions of the SPIOs, we scan with the background

(bias) field slowly decreasing from 60 mT to −60 mT across 0.2s. We have demonstrated the AWR measured 1D PSFs agree with 1D PSFs obtained using our gradient-based imaging systems (Tay, Patrick Goodwill, et al. 2016). To translate the AWR PSF to a true imaging PSF, we only need to divide the DC field by the gradient strength. Reconstruction uses the middle 60 percent of the time-domain signal within a half-period, centered about the sinusoidal zero-crossing in order to maximize SNR. The 60 percent value is chosen to be similar to that used in the Berkeley 3D Magnetic Particle Imager. For Fig. 4, the drive waveform is a 20.25 kHz, 20 mT sine wave to match the drive field of the 3D imaging scanner used. For Fig. 7, the drive frequency and amplitude are as specified in the figure.

2.3. Magnetic Particle Imager Experiments

To verify the findings from the relaxometer experiments, we imaged a point source phantom by lining up 5 tubes (ID 0.7 mm, OD 1.3 mm) with 1 μL of 5 mg/mL SPIO inside each as shown in Fig. 5. We used our 3D MPI scanner with a 7 T/(μ_0m) FFP selection field, comprised of permanent magnet pair. An MPI image is formed by rastering the sensitive field-free-point (FFP) across the entire field-of-view and gridding the received voltage in an inductive pick-up coil to the instantaneous field-free-point position. The FFP is shifted by electromagnetic shift coils in the x and y directions and by the drive coil in z. A robot arm moves the sample in discrete steps in z to compensate for limited amplitude of the transmit coil. The scanning setup is shown in Fig. 2c, where the green trajectory represents the field-free-point location in a y-plane. A homogeneous transmit solenoid adds a 20.25 kHz, 20 mT sine wave excitation along the z-axis, thus making the FFP zigzag (in the z-axis) as it moves along the green trajectory. This is done to sample the regions between the green trajectory lines. The magnetic field gradient is 7 T/(μ_0m) in the x-axis, and 3.5 T/(μ_0m) in the y- and z-axes. The field of view is 14.56 $\times$ 4 $\times$ 3.75 cm^3 and the total scan time is 9 minutes. Details on the 3D MPI scanner hardware and the image reconstruction algorithm have been published (Emine U Saritas et al. 2013; Patrick Goodwill et al. 2012; Lu et al. 2013).

2.4. Calculation of Langevin Spatial resolution curves

In this paper, we use the Houston criterion for spatial resolution (Houston 1927) that uses the full-width-half-maximum of the point spread function or imaging point source. The Langevin spatial resolution (red) curves plotted in Fig. 4 and Fig. 7 was calculated using the equation 4 (Langevin model of an ensemble of ideal magnetic nanoparticles) where the gradient strength G is 3.5 T/(μ_0m) to match the Berkeley Magnetic Particle Imager gradient. We use the experimentally measured nanoparticle $\mu_0 M_{sat}$ value of 0.551 T for these calculations. T is set as 293 K.

3. Results

3.1. Spatial resolution stops improving beyond 25 nm core diameter

The AWR was used to obtain 1D PSFs of Imagion Biosystems PrecisionMRX® nanoparticles with core diameters between 18 to 32 nm. The results in Fig. 3a show that while the PSF narrows when core diameter increases from 18 nm to 24 nm, this trend reverses after 25 nm. This is concomitant with an increasing displacement in the direction of the scan. This behavior is similar to results from prior work (L. R. Croft et al. 2016; L. Croft

et al. 2012) and is indicative of delay between the time-domain MPI signal and the applied field due to increasing magnetic relaxation. This results in blurring of the 1D PSF in the direction of the scan when the time-domain MPI signal is gridded to applied field values during reconstruction. As a result, the improved spatial resolution predicted by the steady-state Langevin PSF is not realized. The steady-state Langevin theory assumes the SPIOs instantaneously respond to the applied field. Fig. 4b shows an increasing disparity between the Langevin model and the experimentally measured spatial resolution as core size increases. For example, the Langevin model predicts that 700 micron resolution is achievable with 32 nm SPIOs, while the experimental resolution achieved was around 7 mm, assuming a 3.5 T/(μ_0m) gradient.

3.2. Verification of trend with MPI imaging results

We confirmed our relaxometer measurement results with an imaging scan using the Berkeley MPI scanner. The images are shown in Fig. 5. The same trend of worsening resolution beyond 24.4 nm is observed and measurement of the FWHM from a line plot (blue dashed line) through the image are in good agreement with the AWR results. The 32.1 nm particles are not visible because the large relaxation time constants leads to very low induced signal in the MPI receive coil $\left(\mathrm{MPI\,signal}\; \propto\; \dfrac{dM}{dt}\right)$. 32.1 nm particles are visible in the relaxometer because a much larger volume ($25\mu L$) is used.

3.3. Magnetic relaxation limits improvement of spatial resolution

To verify that magnetic relaxation is the mechanism behind the limiting of spatial resolution as core size increases, the raw time-domain signal across a half-period of drive field was investigated. Any magnetic relaxation will cause a delay of the time-domain signal in the direction of the scan. In Fig. 6a, while an increase in magnetic relaxation can be inferred from the slight delay of the peak going from 18.5 nm to 24.4 nm, the signal peak has an overall narrowing leading to overall better resolution. This suggests that the effect of Langevin physics dominates over magnetic relaxation in this range of core sizes.

From 24.4 nm to 32.1 nm, however, there is a dramatic increase in peak delay (Fig. 6b). The signal is delayed by ~ 6μs and is spread out across almost twice the time as 24.4 nm. These results show that magnetic relaxation is dramatically more significant beyond 24.4 nm and clearly dominates over Langevin physics.

The raw MPI time-domain data shown here also provides an intuitive explanation of worsening resolution. Since the signal is spread out over more time for 27.4 nm and 32.1 nm, the signal is associated with more voxels in x-space reconstruction because *signal*(*t*) is directly gridded to the voxels that the field-free-point bypassed in that time. Similarly, for system matrix reconstruction, a spread-out signal peak corresponds to a steeper decay in the Magnetic Particle Spectrometry spectra and thus a more poorly conditioned system matrix during image reconstruction.

3.4. Strategies for mitigation of magnetic relaxation do not work fully

Prior work has demonstrated that the MPI drive waveform significantly affects the MPI performance of SPIOs (L. R. Croft et al. 2016; Kuhlmann et al. 2015). Here, we investigate if low amplitude and low frequency approaches can help mitigate magnetic relaxation and achieve the Langevin model spatial resolution. For the low amplitude approach, the frequency was kept constant at the original 20.25 kHz while amplitudes of 20.0, 4.0 and 0.5 mT/μ_0 were used. For the low frequency approach, the amplitude was maintained at the original 20 mT/μ_0 while frequencies of 20.25, 2.0 and 0.4 kHz were used.

The results show that low amplitude approaches do not work well at larger core sizes. This can be attributed to the strong field strength dependence of Néel and Brownian time constants as described in equation 5 and (Robert J Deissler et al. 2014; Dieckhoff et al. 2016), where the smaller AC drive amplitudes mean that the time constants remain relatively large throughout the entire AC period. In contrast, low frequency approaches work better at larger core sizes. The spatial resolution minima of the curve is shifted to 27.4 nm at 0.4 kHz and there is significantly improved spatial resolution by almost 2-fold from the optimal resolution at 20 kHz curve. This can be attributed to the fact that the temporal blurring has a lower impact on the time-domain raw MPI signal shape when the drive waveform period is longer, which in turn results in less blurring during image reconstruction as shown by L. R. Croft et al. 2016. Overall, while both approaches help mitigate magnetic relaxation and improve spatial resolution, the general trend of worsening spatial resolution beyond 27.4 nm still remains. Notably, the fact that low frequency approaches work well at core sizes past the minima of the 20 kHz curve while low amplitude approaches do not (relaxation time constants are longer at low fields) lends further credence to the idea that increasing magnetic relaxation from larger core sizes is the main cause of worsening spatial resolution. In essence, these results suggest that magnetic relaxation is a significant spatial resolution barrier that is not easily resolved by current approaches.

Discussion

As shown in Fig. 1, the ideal steady-state Langevin model for an ensemble of nanoparticles predicts a highly desirable cubic improvement in MPI resolution with core size (Rahmer, Weizenecker, et al. 2009; Patrick W Goodwill and Conolly 2010). However, in practice, relaxation-induced blurring of the MPI signal also occurs and is known to also increase with core size as described in equation 5. Blurring of the MPI image by magnetic relaxation (Neel and/or Brownian mechanisms) is a well-known phenomenon that has been shown in prior work for both system matrix (Schmidt et al. 2015) and x-space reconstruction approaches (L. Croft et al. 2012; L. R. Croft et al. 2016). Our key result, shown in Fig. 4, is the first experimental study of SPIOs in aqueous solvent showing the interplay of these two effects resulting in optimal resolution being achieved at 24.4 nm core size, with worsening resolution beyond 24.4 nm. We presented experimental evidence that the resolution improving effect of the ideal Langevin model for an ensemble of particles is increasingly mitigated and dominated by relaxation-induced blurring. For example, in Fig. 6a, it can be observed there is an increase in time-delay of the MPI signal as core size increases from 18.5 nm to 24.4 nm indicating an increasing delay in ensemble magnetization (magnetic

relaxation). Notably, the signal response is still narrower in time for 24.4 nm, suggesting that both the resolution improvement from the Langevin model and relaxation-induced blurring are affecting the MPI signal.

While magnetic core size is a major factor in influencing the Neel and Brownian relaxation time constants as described in equation 5, there are other factors that may affect these time constants and therefore the MPI resolution. One possible factor is the shape anisotropy constant. While the particles used in this study are all spherical, larger core sizes are slightly less so (see Fig. 3a). However, the maximum shape anisotropy calculated from this factor is $2341 Jm^{-3}$ which is only a small fraction (<0.172) compared to the magnetocrystalline anisotropy. Equation 10 and 11 of Graeser et al. 2015 and magnetocrystalline anisotropy of magnetite $K_1 = -13600 Jm^{-3}$ was used. Therefore, the increase in shape anisotropy contributes only minimally and cannot be solely responsible for the two-fold worsening of spatial resolution between 24.4 nm and 32.1 nm particles. Another possible factor is the changing hydrodynamic sizes between different core sizes (see Fig. 3a). Hydrodynamic size has a large impact on the Brownian relaxation time constant but is does not affect the Néel relaxation time constant (equation 5). While there is a poor correlation between the measured hydrodynamic size and measured MPI resolution for the 18.5 – 24.4 nm range of particles, the correlation is better for the 24.4 – 32.1 nm range of particles. The results suggests that the impact of hydrodynamic size on MPI resolution is modulated by the relative dominance of Néel and Brownian relaxation mechanisms which in turn is most dependent on magnetic core size due to the exponential dependence of the Néel time constant on the magnetic core volume. While it is possible that hydrodynamic size contributes towards the worsening resolution going from 24.4 nm to 32.1 nm and that better resolution could be obtained with very thin coatings, in practice, a minimum coating thickness is required in synthesis for successful phase transfer as well as to prevent spontaneous aggregation of nanoparticles. Yet another factor to consider is the width of the particle size distribution. From Knopp et al. 2011, there is less than a two-fold improvement in resolution of the normalized convolution kernel between a 15 nm monosized ensemble and a polysized ensemble (lognormal with 16.4 nm mean with 4 nm standard deviation). For the particles used in this study, the standard deviation is constant at 1.5 nm and only increases to 2.1 and 2.2 nm at 27.6 nm and 32.1 nm core sizes respectively (see Fig. 3a). The variation in size distribution for this study is thus much lower than that shown by Knopp et al., and therefore this factor can be considered to contribute only minimally to the spatial resolution trend measured in this study.

The results of our study show that with current typical MPI imagers operating around 20 kHz and 20 mT drive amplitude, spatial resolution on a typical 7 T/(μ_0m) gradient is limited to about 1.5 mm. For preclinical applications, this spatial resolution is not ideal. This is especially so for smaller rodents such as mice and also when investigating disease models of the vasculature. This resolution challenge of MPI is valid with both methods of reconstructing the MPI image. For example, Weizenecker and Rahmer's 2009 landmark paper on the System Matrix (Rahmer, Weizenecker, et al. 2009) noted that while a 5.5 T/(μ_0m) gradient and dominant particle diameter of 30 nm theoretically allows a resolution better than 0.5 mm, experimentally, due to the wide distribution of particle sizes and the

regularization applied in reconstruction to mitigate limited SNR, the observed resolution was not better than 1.5 mm.

Many approaches have been taken to improve the spatial resolution of MPI. One approach is to increase the gradient strength of the MPI imager (Vogel et al. 2015; E. Y. Yu et al. 2015; P Goodwill et al. 2015). Gradients of up to 7 T/(μ_0m) have been achieved on murine scanners at Berkeley (E. Y. Yu et al. 2015; P Goodwill et al. 2015). Notably, Vogel et al. 2015 achieved a gradient strength of 85 T/(μ_0m) which will theoretically achieve 29 μm resolution with a 30 nm magnetite core particle (assuming instantaneous relaxation). However, the bore size of the device is very small (6 mm diameter) and cannot fit small animals. Such high gradients for a small animal-sized bore would require superconducting magnets, with increased cost and complexity. In addition, the high gradients imply that the rate of scanning across the entire field-of-view will have to be proportionally slowed down due to obey magnetostimulation and SAR safety limits (E U Saritas et al. 2013). Finally, as demonstrated in Fig. 1, like MRI, the spatial resolution of MPI improves only *linearly* with increasing gradient strength.

Deconvolution approaches could potentially obtain significant spatial resolution improvements. However, our knowledge of the *in vivo* PSF and relaxation behavior is imperfect, and also the conditioning of the computation could damage final SNR, especially with relaxation-induced blurring of the MPI signal. The fundamental SNR versus resolution tradeoffs with sophisticated deconvolution algorithms has been studied specifically for MPI by Knopp et al. 2011 and in general by Shahram et al. 2004.

Other approaches include optimizing the drive waveform to mitigate the blurring effects of magnetic relaxation. Notably, low amplitude or low frequency approaches have been investigated before (L. R. Croft et al. 2016; Kuhlmann et al. 2015; Murase, Hiratsuka, et al. 2014; Shah et al. 2014). In our study, we tested out these strategies on our range of magnetic core sizes. Unfortunately, while some improvement in spatial resolution was observed, Fig. 7 shows that neither approach is able to fully mitigate the blurring from magnetic relaxation in order to achieve the theoretical Langevin spatial resolution for larger core sizes. Very low frequencies (<400 Hz) could show promise for MPI, but MPI uses an inductive pick-up coil today, so SNR will be reduced. SQUID detectors have SNR independent of frequency, so they may mitigate this challenge.

Perhaps the most promising approach is to optimize novel magnetic nanoparticle tracers for great resolution and minimal relaxation-induced blurring (Ferguson, Minard, et al. 2009; Ferguson, Khandhar, Minard, et al. 2010; Ferguson, Khandhar, and Krishnan 2012; Hufschmid et al. 2015). Here, the nanoparticle synthesis will involve attention to particle phase purity. Furthermore, as Weizenecker et al. 2012 has shown, optimizing the particle anisotropy can prove valuable. In addition, Graeser et al. 2015 has shown that superimposing of shape semi-axis and crystal axes during crystal growth can improve the MPI performance. For very large core sizes, because the Néel time constant is larger than Brownian time constant for low applied fields (Robert J Deissler et al. 2014), Brownian relaxation will be dominant. Hence, tailored SPIOs with the smallest hydrodynamic radius possible while still

maintaining a thick enough coating to prevent aggregation may also show resolution improvements.

Conclusions

In this study, we perform the first experimental study on the interplay of Langevin steady-state physics and magnetic relaxation as particle core size is increased and measure its effects on MPI spatial resolution. The experimental results show that magnetic relaxation limits the optimal core size of MPI nanoparticle tracers to ~ 25 nm. We experimentally observe a significant disparity, consistent with trends from prior modeling work, between the resolution predicted by the steady-state Langevin physics model and that achieved experimentally for SPIOs with core size larger than 25 nm. For example, the steady-state Langevin predicts ~ 600 micron resolution with a 3.5 T/(μ_0m) gradient and 32 nm SPIO, but experimentally ~ 7 mm resolution is achieved. This spatial resolution disparity remains even after optimizing the drive waveform to reduce the impact of relaxation-induced blurring, suggesting that magnetic relaxation is a potent and unresolved barrier to unlocking the potential of large core size particles. We hope that in the near future, MPI researchers will invent new methods to overcome magnetic relaxation-induced blurring for larger core sizes. This will allow us to unlock the highly desirable cubic improvement of MPI spatial resolution with nanoparticle core size.

Acknowledgments

References

Croft, Laura R., Goodwill, Patrick W., Konkle, Justin J., Arami, Hamed, Price, Daniel A., Li, Ada X., Saritas, Emine U., Conolly, Steven M. Low drive field amplitude for improved image resolution in magnetic particle imaging. Medical physics. 2016; 43(1):424–435. [PubMed: 26745935]

Croft, Laura, Goodwill, Patrick, Conolly, Steven. Relaxation in x-space magnetic particle imaging. IEEE Trans Med Imaging. 2012; 31(12):2335–2342. [PubMed: 22968211]

Cullity, BD., Graham, CD. Introduction to Magnetic Materials. John Wiley & Sons; 2011.

Deissler RJ, Martens MA. Dependence of the Magnetization Response on the Driving Field Amplitude for Magnetic Particle Imaging and Spectroscopy. IEEE Trans Magn. 2015; 51(2):1–4. [PubMed: 26203196]

Deissler, Robert J., Wu, Yong, Martens, Michael A. Dependence of Brownian and Néel relaxation times on magnetic field strength. Med Phys. 2014; 41(1):012301. [PubMed: 24387522]

Dhavalikar R, Hensley D, Maldonado-Camargo L, Croft LR, Ceron S, Goodwill PW, Conolly SM, Rinaldi C. Finite magnetic relaxation in x-space magnetic particle imaging: comparison of measurements and ferrohydrodynamic models. Journal of Physics D: Applied Physics. 2016; 49(30):305002. [PubMed: 27867219]

Dieckhoff, Jan, Eberbeck, Dietmar, Schilling, Meinhard, Ludwig, Frank. Magnetic-field dependence of Brownian and Néel relaxation times. J Appl Phys. 2016; 119(4):043903.

Ferguson, R Matthew, Khandhar, Amit P., Krishnan, Kannan M. Tracer design for magnetic particle imaging. J Appl Phys. 2012; 111(7):07B318.

Ferguson, R Matthew, Khandhar, Amit P., Minard, Kevin R., Krishnan, Kannan M. Magnetic Nanoparticles. WORLD SCIENTIFIC; 2010. SIZE-OPTIMIZED MAGNETITE NANOPARTICLES FOR MAGNETIC PARTICLE IMAGING; p. 53-59.

Ferguson, R Matthew, Minard, Kevin R., Krishnan, Kannan M. Optimization of nanoparticle core size for magnetic particle imaging. J Magn Magn Mater. 2009; 321(10):1548–1551. [PubMed: 19606261]

Fidler F, Steinke M, Kraupner A, Gruttner C, Hiller K-H, Briel A, Westphal F, Walles H, Jakob PM. Stem Cell Vitality Assessment Using Magnetic Particle Spectroscopy. IEEE Trans Magn. 2015; 51(2):1–4. [PubMed: 26203196]

García-Palacios, José Luis, Lázaro, Francisco J. Langevin-dynamics study of the dynamical properties of small magnetic particles. Phys Rev B Condens Matter. 1998; 58(22):14937–14958.

Gleich, Bernhard, Weizenecker, Jurgen. Tomographic imaging using the nonlinear response of magnetic particles. Nature. 2005; 435:1214–1217. issn: 7046. url: http://dx.doi.org/10.1038/nature03808. DOI: 10.1038/nature03808 [PubMed: 15988521]

Goodwill, Patrick W., Conolly, Steven M. The X-space formulation of the magnetic particle imaging process: 1-D signal, resolution, bandwidth, SNR, SAR, and magnetostimulation. IEEE transactions on medical imaging. 2010; 29(11):1851–1859. [PubMed: 20529726]

Goodwill, Patrick W., Konkle, Justin J., Zheng, Bo, Saritas, Emine U., Conolly, Steven M. Projection x-space magnetic particle imaging. IEEE Trans Med Imaging. 2012; 31(5):1076–1085. [PubMed: 22552332]

Goodwill, Patrick W., Lu, Kuan, Zheng, Bo, Conolly, Steven M. An x-space magnetic particle imaging scanner. Rev Sci Instrum. 2012; 83(3):033708. [PubMed: 22462930]

Goodwill, Patrick, Croft, Laura, Konkle, Justin, Lu, Kuan, Saritas, Emine, Zheng, Bo, Conolly, Steven. Third Generation X-Space MPI Mouse and Rat Scanner. In: Buzug, Thorsten M., Borgert, Jörn, editors. Magnetic Particle Imaging. Springer; Berlin Heidelberg: 2012. p. 261-265.Springer Proceedings in Physics

Goodwill P, et al. In Vivo and Ex vivo experimental MPI angiography with high selection field strength and tailored SPIO nanoparticles. Magnetic Particle Imaging (IWMPI), 2015 5th International Workshop on ieeexplore.ieee.org. 2015:1–1.

Graeser M, Bente K, Buzug TM. Dynamic single-domain particle model for magnetite particles with combined crystalline and shape anisotropy. J Phys D Appl Phys. 2015; 48(27):275001.

Haegele, Julian, Rahmer, Jürgen, Gleich, Bernhard, Borgert, Jörn, Wojtczyk, Hanne, Panagiotopoulos, Nikolaos, Buzug, Thorsten M., Barkhausen, Jörg, Vogt, Florian M. Magnetic particle imaging: visualization of instruments for cardiovascular intervention. Radiology. 2012; 265(3):933–938. [PubMed: 22996744]

Hensley, Daniel W., Tay, Zhi Wei, Dhavalikar, Rohan, Zheng, Bo, Goodwill, Patrick, Rinaldi, Carlos, Conolly, Steven. Combining magnetic particle imaging and magnetic fluid hyperthermia in a theranostic platform. Phys Med Biol. 2016

Houston, William V. A Compound Interferometer for Fine Structure Work. Phys Rev. 1927; 29(3):478–484.

Hufschmid, Ryan, Arami, Hamed, Ferguson, R Matthew, Gonzales, Marcela, Teeman, Eric, Brush, Lucien N., Browning, Nigel D., Krishnan, Kannan M. Synthesis of phase-pure and monodisperse iron oxide nanoparticles by thermal decomposition. Nanoscale. 2015; 7(25):11142–11154. [PubMed: 26059262]

Knopp, Tobias, Biederer, Sven, Sattel, Timo F., Erbe, Marlitt, Buzug, Thorsten M. Prediction of the spatial resolution of magnetic particle imaging using the modulation transfer function of the imaging process. IEEE Trans Med Imaging. 2011; 30(6):1284–1292. [PubMed: 21317081]

Kuhlmann C, Khandhar AP, Ferguson RM, Kemp S, Wawrzik T, Schilling M, Krishnan KM, Ludwig F. Drive-Field Frequency Dependent MPI Performance of Single-Core Magnetite Nanoparticle Tracers. IEEE Trans Magn. 2015; 51(2):1–4. [PubMed: 26203196]

Lu, Kuan, Goodwill, Patrick W., Saritas, Emine U., Zheng, Bo, Conolly, Steven M. Linearity and shift invariance for quantitative magnetic particle imaging. IEEE transactions on medical imaging. 2013; 32(9):1565–1575. [PubMed: 23568496]

Ludwig F, Wawrzik T, Yoshida T, Gehrke N, Briel A, Eberbeck D, Schilling M. Optimization of Magnetic Nanoparticles for Magnetic Particle Imaging. IEEE Trans Magn. 2012; 48(11):3780–3783.

Murase, Kenya, Aoki, Marina, Banura, Natsuo, Nishimoto, Kohei, Mimura, Atsushi, Kuboyabu, Tomomi, Yabata, Isamu. Usefulness of Magnetic Particle Imaging for Predicting the Therapeutic Effect of Magnetic Hyperthermia. Open Journal of Medical Imaging. 2015; 5(02):85.

Murase, Kenya, Hiratsuka, Samu, Song, Ruixiao, Takeuchi, Yuki. Development of a system for magnetic particle imaging using neodymium magnets and gradiometer. Jpn J Appl Phys. 2014; 53(6):067001.

Nishimoto, Kohei, Mimura, Atsushi, Aoki, Marina, Banura, Natsuo, Murase, Kenya. Application of Magnetic Particle Imaging to Pulmonary Imaging Using Nebulized Magnetic Nanoparticles. Open Journal of Medical Imaging. 2015; 5(02):49.

Orendorff, Ryan, Wendland, Michael, Yu, Elaine, Zheng, Bo, Goodwill, Patrick, Conolly, Steve. 2016 World Molecular Imaging Congress (WMIC 2016): Imaging Biology… Improving Therapy. World Molecular Imaging Society (WMIS); 2016. First in vivo Brain Perfusion Imaging using Magnetic Particle Imaging.

Rahmer J, Halkola A, Gleich B, Schmale I, Borgert J. First experimental evidence of the feasibility of multi-color magnetic particle imaging. Phys Med Biol. 2015; 60(5):1775–1791. [PubMed: 25658130]

Rahmer J, Weizenecker Jürgen, Gleich Bernhard, Borgert Jörn. Signal encoding in magnetic particle imaging: properties of the system function. BMC Med Imaging. 2009; 9:4. [PubMed: 19335923]

Salamon, Johannes, et al. Magnetic Particle/Magnetic Resonance Imaging: In-Vitro MPI-Guided Real Time Catheter Tracking and 4D Angioplasty Using a Road Map and Blood Pool Tracer Approach. PLoS One. 2016; 11(6):e0156899. [PubMed: 27249022]

Saritas EU, Goodwill PW, Zhang GZ, Conolly SM. Magnetostimulation Limits in Magnetic Particle Imaging. IEEE Trans Med Imaging. 2013; 32(9):1600–1610. [PubMed: 23649181]

Saritas, Emine U., Goodwill, Patrick W., Croft, Laura R., Konkle, Justin J., Lu, Kuan, Zheng, Bo, Conolly, Steven M. Magnetic particle imaging (MPI) for NMR and MRI researchers. J Magn Reson. 2013; 229:116–126. [PubMed: 23305842]

Schmidt D, Palmetshofer F, Heinke D, Steinhoff U, Ludwig F. A Phenomenological Description of the MPS Signal Using a Model for the Field Dependence of the Effective Relaxation Time. IEEE Trans Magn. 2015; 51(2):1–4. [PubMed: 26203196]

Shah, Saqlain A., Ferguson, RM., Krishnan, KM. Slew-rate dependence of tracer magnetization response in magnetic particle imaging. J Appl Phys. 2014; 116(16):163910. [PubMed: 25422528]

Shahram, Morteza, Milanfar, Peyman. Imaging Below the Diffraction Limit: A Statistical Analysis. IEEE Trans ON Image Processing. 2004:13.

Tay, Zhi Wei, Goodwill, PW., Hensley, DW., Conolly, S. Untuned MPI relaxometer for nanoparticle characterization at arbitrary frequencies. Magnetic Particle Imaging (IWMPI), 2015 5th International Workshop on. 2015:1–1.

Tay, Zhi Wei, Goodwill, Patrick, Hensley, Daniel, Taylor, Laura, Zheng, Bo, Conolly, Steven. A High-Throughput, Arbitrary-Waveform, MPI Spectrometer and Relaxometer for Comprehensive Magnetic Particle Optimization and Characterization. Scientific reports. 2016:6. [PubMed: 28442741]

Them, Kolja, Salamon, J., Szwargulski, P., Sequeira, S., Kaul, MG., Lange, C., Ittrich, H., Knopp, Tobias. Increasing the sensitivity for stem cell monitoring in system-function based magnetic particle imaging. Phys Med Biol. 2016; 61(9):3279–3290. [PubMed: 27032447]

Vogel, Patrick, Ruckert, Martin, Jakob, Peter M., Behr, Volker C., et al. MPI—Initial Experiments With an Ultrahigh Resolution MPI. IEEE Trans Magn. 2015; 51(2):1–4. [PubMed: 26203196]

Vreeland, Erika C., et al. Enhanced Nanoparticle Size Control by Extending LaMers Mechanism. Chem Mater. 2015; 27(17):6059–6066.

Weizenecker, Jürgen, Gleich, Bernhard, Rahmer, Jürgen, Borgert, Jörn. Magnetic Nanoparticles. WORLD SCIENTIFIC; 2010. PARTICLE DYNAMICS OF MONO-DOMAIN PARTICLES IN MAGNETIC PARTICLE IMAGING; p. 3-15.

Weizenecker, Jürgen, Gleich, Bernhard, Rahmer, Jürgen, Borgert, Jörn. Micro-magnetic simulation study on the magnetic particle imaging performance of anisotropic mono-domain particles. Phys Med Biol. 2012; 57(22):7317. [PubMed: 23079678]

Yu, EY., Goodwill, PW., Conolly, SM. Preliminary characterization of a laminated iron-core 6.3 T/m FFL magnet; Magnetic Particle Imaging (IWMPI), 2015 5th International Workshop on. 2015. p. 1-1.ieeexplore.ieee.org

Yu, Elaine, Bishop, Mindy, Zheng, Bo, Ferguson, Matt, Khandhar, Amit, Kemp, Scott, Krishnan, Kannan, Goodwill, Patrick, Conolly, Steve. 2016 World Molecular Imaging Congress (WMIC 2016): Imaging Biology… Improving Therapy. World Molecular Imaging Society (WMIS); 2016. First demonstration of in vivo Cancer Magnetic Particle Imaging with IV-administered Passive Long-circulating SPIOs.

Zheng, Bo, Vazin, Tandis, Goodwill, Patrick, Conway, Anthony, Verma, Aradhana, Saritas, Emine, Schaffer, David, Conolly, Steven. Magnetic Particle Imaging tracks the long-term fate of in vivo neural cell implants with high image contrast. Sci Rep. 2015; 5:14055. [PubMed: 26358296]

Zheng, Bo, von See, Marc, Yu, Elaine, Gunel, Beliz, Lu, Kuan, Vazin, Tandis, Schaffer, David V., Goodwill, Patrick W., Conolly, Steven M. Quantitative Magnetic Particle Imaging Monitors the Transplantation, Biodistribution, and Clearance of Stem Cells In Vivo. Theranostics. 2016; 6:291–301. issn: 3. url: http://www.ncbi.nlm.nih.gov/pmc/articles/PMC4737718/. DOI: 10.7150/thno. 13728 [PubMed: 26909106]

Zhou, Xinyi, Yu, Elaine, Keselman, Paul, Goodwill, Patrick, Nahid, Payam, Zheng, Bo, Conolly, Steve. 2016 World Molecular Imaging Congress (WMIC 2016): Imaging Biology… Improving Therapy. World Molecular Imaging Society (WMIS); 2016. In Vivo Magnetic Particle Imaging of Lung Perfusion in Rats - Towards High Sensitivity and High Contrast Non-Radiation Based Diagnostics for Pulmonary Embolism.
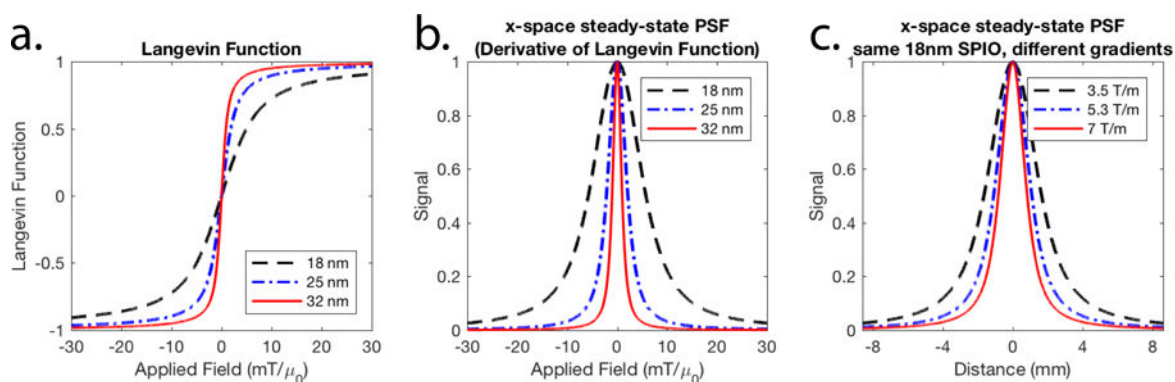
Figure 1.
(a) Calculated Langevin curves (using eqn. 3) for different nanoparticle core sizes. The shape of the curves show a dramatic change with nanoparticle core size due to the cubic relationship between nanoparticle core size and saturation field. (b) Calculated MPI steady-state PSFs show a dramatic narrowing with increased core size. This is in contrast to the strategy of increasing MPI gradient strength shown in (c) where only a linear improvement of the PSF width is observed with increases in gradient strength. Because spatial encoding in MPI is a linear function of the magnetic field gradient, conversion between x-axis units of applied field (mT/μ_0) and distance (mm) is done simply by dividing by the gradient strength (T/μ_0m).
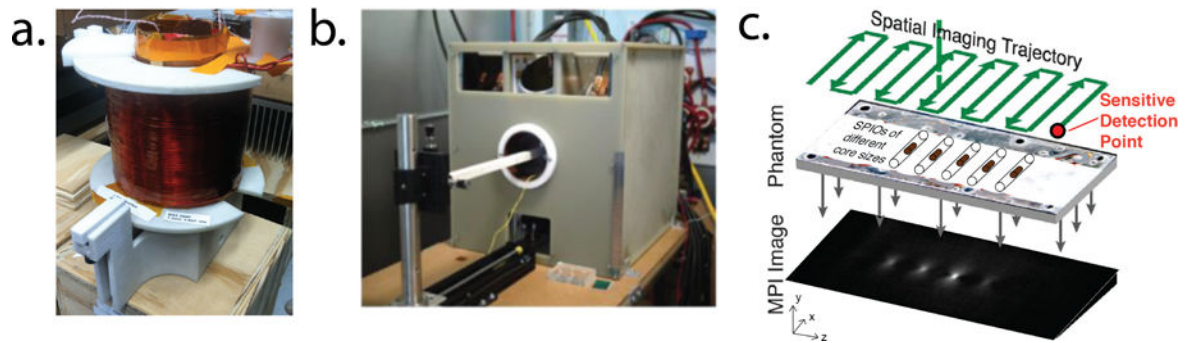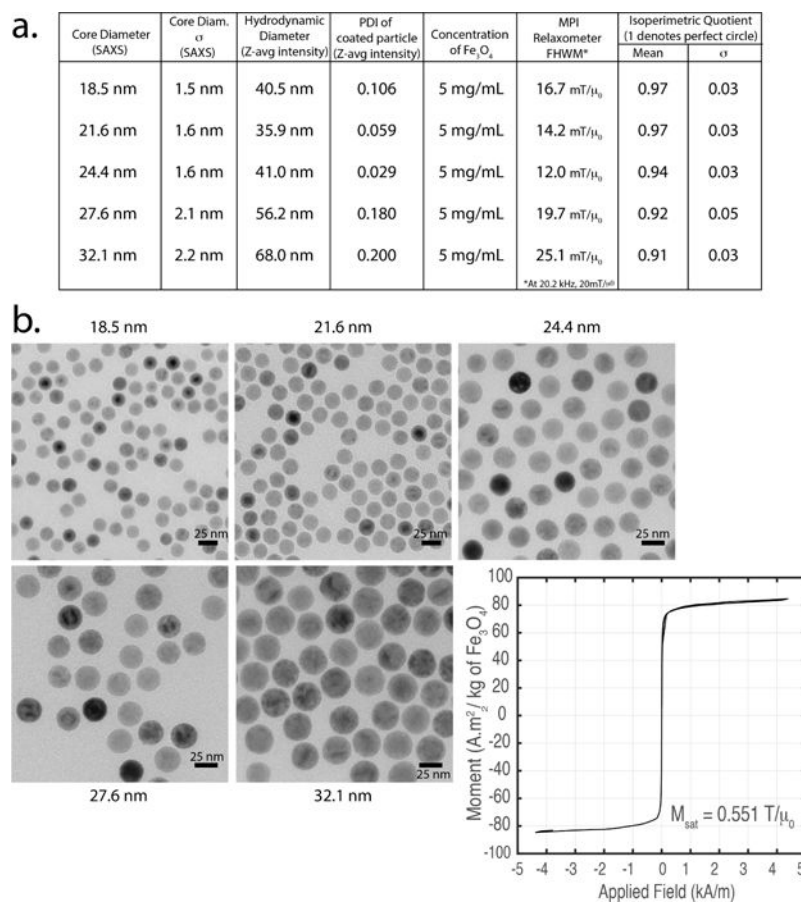
Figure 2.
MPI hardware. (a) Magnetic Particle Relaxometer used to obtain point spread functions of SPIOs to measure the full-width-at-half-maximum spatial resolution. (b) Magnetic Particle Imager used to obtain images of SPIOs to validate the measurements of the relaxometer as well as provide visual images of the differences in spatial resolution as core size changes. (c) MPI obtains an image by rastering the field-free-point across the field of view as shown in the figure. The field-free-point can be considered a sensitive detection point in 3D space. In x-space reconstruction, the time-domain received voltage signal is gridded to the instantaneous location of the field-free-point to make an image.

Figure 3.
(a) Table of nanoparticle properties and experimental measurements (b) TEM of Imagion Biosystems PrecisionMRX® SPIOs showing narrow size variation and constant spherical shape as evidenced by the isoperimetric quotients (thus implying constant shape anisotropy). A representative M vs. H plot ($M_{sat} = 0.551 \, T/\mu_0$) is also plotted. See Section 2.1 for more details.
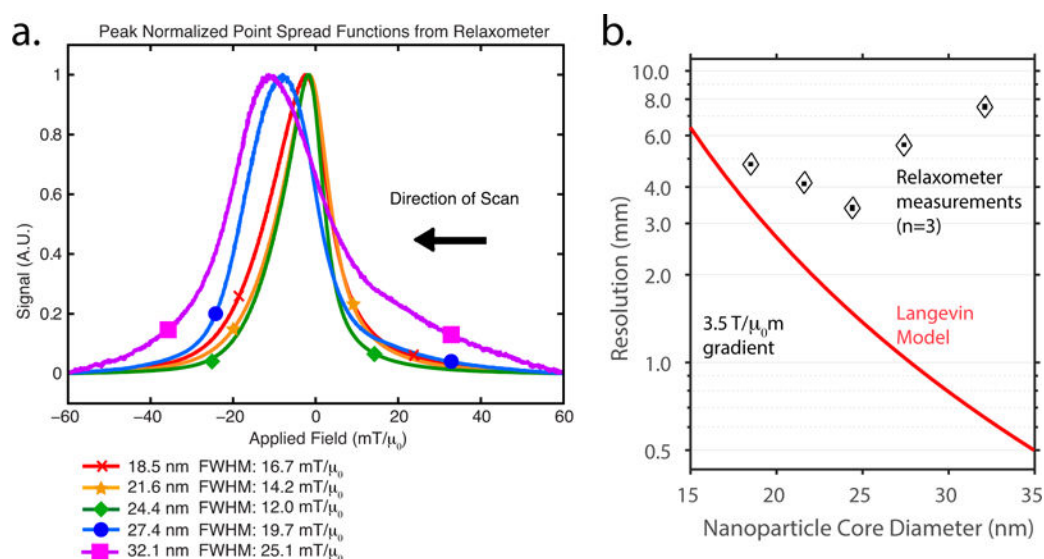
Figure 4.

(a) Experimental 1D point spread functions of Imagion Biosystems PrecisionMRX®SPIOs measured on the Magnetic Particle Relaxometer at 20.25 kHz and 20 mT/μ_0. The PSF narrows as core size increases from 18 to 24 nm, but stops narrowing and starts widening beyond 25 nm. This shift is concomitant with a marked displacement of the PSF in the direction of the scan which is similar to that seen in prior work on MPI relaxation (L. R. Croft et al. 2016; L. Croft et al. 2012), suggesting a marked increase in magnetic relaxation processes. Data is represented by the smooth solid lines while the markers are just a visual guide to differentiate the curves. (b) Comparison of the experimentally achieved spatial resolution (n = 3) with the predicted spatial resolution from the Langevin model shows an increasing disparity with increasing core size after 24.4 nm.
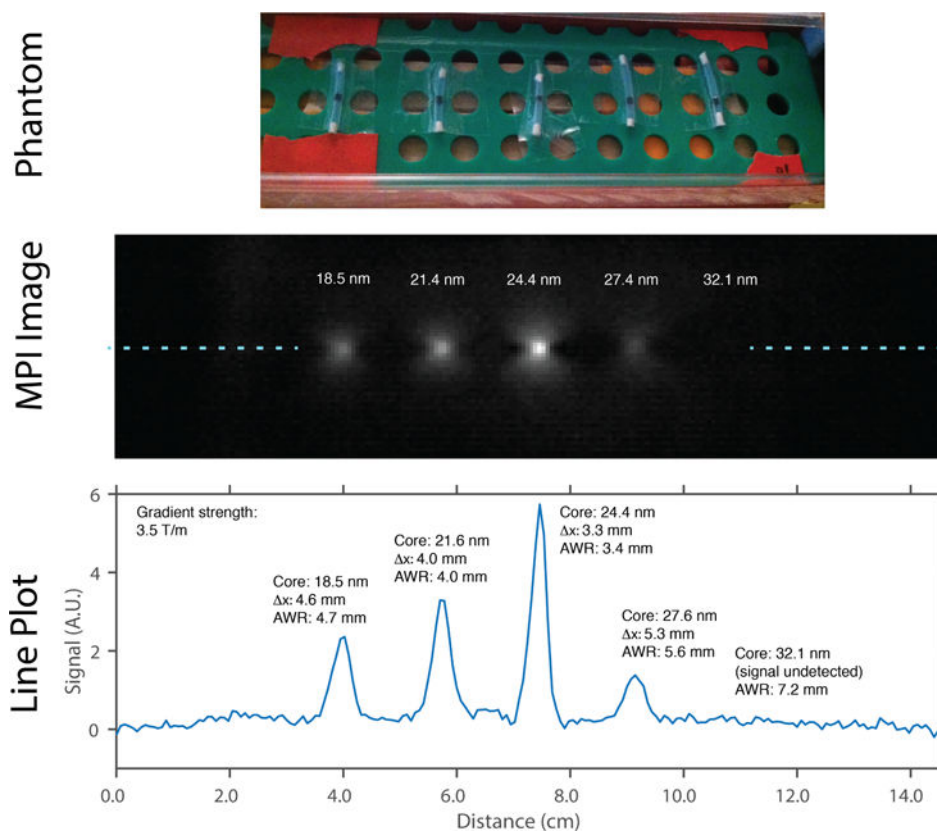
Figure 5.
Magnetic Particle Imager scan of point sources of different SPIO core sizes. The experimental imaging results have good agreement with the Relaxometer measurements, showing the same trend of optimal resolution with 24.4 nm SPIOs.
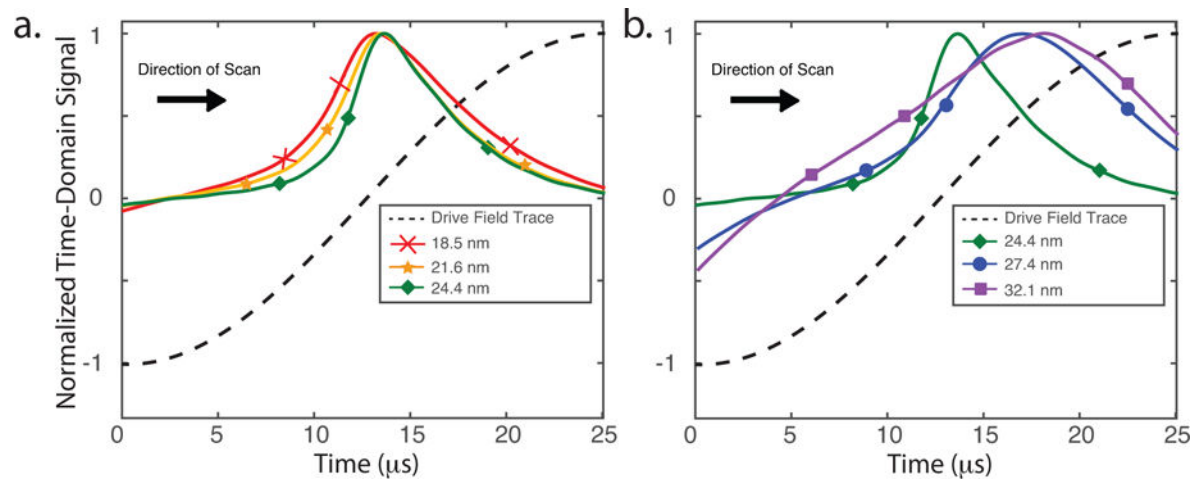
Figure 6.

Trace of the *experimental* time-domain MPI signal. Data is represented by the smooth solid lines while the markers are just a visual guide to differentiate the curves. a) From 18.5 nm to 24.4 nm, a slight increase in delay is seen in the peaks of each subsequent trace. This is indicative of magnetic relaxation processes increasing in magnitude. However, this effect is surpassed by the narrowing of the signal peak by Langevin physics. Thus, the narrowest peak and best resolution is seen at 24.4 nm. b) From 24.4 nm to 32.1 nm however, magnetic relaxation increases dramatically as evidenced by the very large time delay (phase delay of almost 40 degrees) of the 27.4 nm and 32.1 nm signal peaks. This is indicative of strong magnetic relaxation processes that clearly dominate the expected peak narrowing from Langevin physics. As a result, the signal peak is spread out and worse resolution occurs when going from 24.4 nm to 32.1 nm.
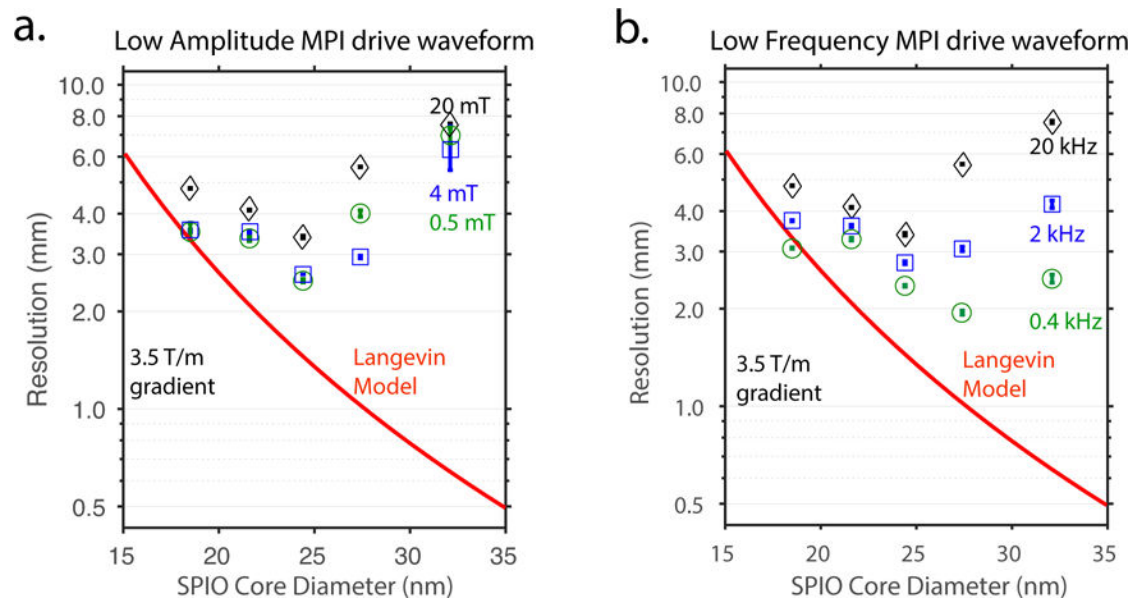
Figure 7.
Low amplitude and low frequency drive waveform strategies have been shown in prior work to reduce the negative impact of magnetic relaxation (Kuhlmann et al. 2015; L. R. Croft et al. 2016). Both approaches were tested separately (n=3, error bars are small and within the shape markers). (a) In the low amplitude approach, frequency is held constant at 20.25 kHz and amplitudes of 20.0, 4.0 and 0.5 mT/μ_0 were used. (b) The low frequency approach keeps amplitude constant at 20 mT/μ_0 while frequencies of 20.25, 2.0 and 0.4 kHz were used. While both strategies help achieve better spatial resolution overall, spatial resolution still stops improving after a certain core size. These strategies are unable to fully mitigate the negative impact of the large amount of relaxation seen by larger core size particles and are unable to achieve the cubic spatial resolution improvements predicted by the Langevin model.